

Towards exascale fully relativistic pseudopotential density functional theory calculations enabled by mixed-precision computation and compressed-communication using residual based subspace iteration

Nikhil Kodali*, Gourab Panigrahi*, Nishant Gupta*, Kartick Ramakrishnan*, Sundaresan G*, Rudra Panch*, Sambit Das[†], Vishwas Rao[‡], Phani Motamarri*[§]

*Department of Computational and Data Sciences, Indian Institute of Science, Bangalore, India

[†]Department of Mechanical Engineering, University of Michigan, Ann Arbor, USA

[‡]Argonne National Laboratory, Lemont, IL, USA

[§]Corresponding author: phanim@iisc.ac.in

Abstract—Noncollinear (NC) magnetism and spin-orbit coupling (SOC) are indispensable for predictive *ab initio* materials simulations with pronounced relativistic effects and magnetic frustration, yet they significantly increase the cost of cubic-scaling density functional theory (DFT) by introducing complex 2-component wavefunctions per electron and consequently much larger eigenproblems. We present a GPU-centric high-performance framework for NC-SOC DFT that combines: (i) algorithmic advances for solving finite-element (FE) discretized DFT equations; (ii) residual-based Chebyshev filtered subspace iteration (R-ChFSI), tolerant to inexact matrix-vector products, for the resulting sparse generalized eigenproblem; (iii) a matrix-free strategy for accelerating FE Poisson solver; (iv) R-ChFSI-enabled mixed-precision computation with block floating-point compressed MPI communication at compression ratios over 4x, preserving double-precision robustness while reducing compute and data movement costs; and (v) a communication efficient band-partitioning algorithm to improve scalability. Numerical results demonstrate improved time-to-solution and excellent scaling on exascale architectures, enabling fully relativistic pseudopotential DFT simulations of up to 100,000 electrons.

I. INTRODUCTION

Understanding the quantum mechanical behaviour of electrons in molecules and materials lies at the heart of modern computational science. Electronic structure methods — ranging from configuration interaction (CI) and quantum Monte Carlo (QMC) to density functional theory (DFT) — have become indispensable tools for predicting and interpreting the properties of complex molecular and materials systems, and have been the subject of several past Gordon Bell winners [1]–[5] and finalists [6], [7]. Among these, DFT [8], [9] stands out as the method of choice for large-scale quantum simulations, striking a compelling balance between computational efficiency and predictive accuracy. In particular, DFT offers a formally exact reduction of the otherwise intractable interacting many-electron Schrödinger equation to an equivalent problem of non-interacting electrons in an effective mean-field dependent on the electron density ($\rho(\mathbf{r})$). In other words, DFT reduces the complexity from $\mathcal{O}(e^{N_e})$ to $\mathcal{O}(N_e^3)$ (N_e denoting the number of electrons)—a momentous advance that has been honoured with the *Nobel Prize* in Chemistry in 1998 [10].

Complex magnetic materials with heavy elements exhibit pronounced anisotropy in magnetism, with the spin quantization axis varying from site to site, a phenomenon known

as noncollinear (NC) magnetism. In such systems, spin-orbit coupling (SOC), a relativistic effect coupling the electron spin to its orbital motion, governs the interaction between magnetic moments and the crystal lattice, stabilising noncollinear magnetic structures. Beyond magnetic systems, SOC induces exotic electronic behaviour in non-magnetic materials by lifting band degeneracies, leading to phenomena such as band splitting and the stabilization of topological phases. Large-scale NC-SOC-DFT simulations are essential for understanding spin textures such as skyrmions and spin spirals, the nonlinear Hall effect in incommensurate Moiré lattices, anomalous transport in topological semimetals, magnetocrystalline anisotropy in rare-earth permanent magnets with point defects and many more. Predictive simulations of these phenomena are key to the rational design of spintronic devices including spin-transfer torque memories, racetrack storage, and spin-logic architectures, as well as topological qubits for fault-tolerant quantum computing and energy-efficient spin-based electronics that overcome the power limitations of conventional charge-based CMOS technology. Generalizing Kohn-Sham DFT to incorporate noncollinear magnetism (NC) and SOC is far from trivial: it requires complex two-component spinor wavefunctions per electron, doubling both the size of the Hamiltonian and the number of eigenpairs to be computed in complex arithmetic. This significantly increases the computational prefactor relative to standard DFT and drives the system to the asymptotic cubic-scaling regime at much smaller system sizes, severely restricting accessible system sizes to typically ~ 500 – 2000 electrons in state-of-the-art NC-SOC-DFT calculations.

Efforts to circumvent the cubic-scaling bottleneck have focused on linear-scaling or reduced scaling approaches that exploit the nearsightedness of electronic interactions [11]–[15], as well as stochastic DFT methods [16], [17]. However, these approaches are not well-suited for metallic systems, where the nearsightedness principle breaks down, and furthermore the robustness of these techniques has not been demonstrated for material systems exhibiting noncollinear magnetism and spin-orbit coupling. Consequently, a systematically convergent and broadly applicable computational framework that reduces the pre-factor for conducting large-scale NC-SOC-DFT on modern GPU-accelerated exascale architectures remains an open challenge. Compounding this, modern GPU architec-

tures are increasingly optimized for low-precision arithmetic, offering substantially higher floating-point throughput at reduced precision compared to double precision. Yet scientific computing demands high accuracy, making it imperative to develop algorithms that harness the performance gains of low-precision computation while preserving the robustness of double-precision results.

Addressing the above challenges, we present a significant advance in the state of the art for NC-SOC-DFT calculations through a real-space computational framework that combines several algorithmic and HPC innovations applicable to both metallic, semi-conducting and insulating systems. This is realised by bringing together the following ideas: (i) an efficient adaptive spatial discretisation through higher-order finite elements (FE), (ii) a GPU-accelerated conjugate gradient solver using a novel matrix-free implementation strategy for the Poisson problem in DFT electrostatics; (iii) residual-based Chebyshev filtered subspace iteration (R-ChFSI), tolerant to inexact matrix-vector products, for solving the resulting large, sparse generalized eigenproblem; (iv) mixed-precision computation and block floating-point compressed MPI communication, both enabled by R-ChFSI, preserving double-precision robustness while reducing compute and data movement costs; and (v) a communication-efficient band-partitioning algorithm to improve strong scalability on multinode GPU architectures at extreme scaling. The proposed framework enables NC-SOC-DFT calculations on systems with $\mathcal{O}(10^5)$ electrons, a significant advance over the $\mathcal{O}(10^2 - 10^3)$ electrons currently accessible using NC-SOC-DFT calculations using pseudopotentials. We implement our framework in the electronic structure package DFT-FE [7], [18] and evaluate it on the exascale supercomputer Aurora (Intel GPUs), for both semiconducting and metallic systems exhibiting noncollinear magnetism and spin-orbit coupling. In particular, we demonstrate our innovations on two scientifically important systems: heavy-element twisted bilayers of transition metal dichalcogenide MoSe₂ (semi-conducting) and the van der Waals system Fe₃GeTe₂ (metallic), where large supercells and heavy atomic species make NC-SOC-DFT calculations particularly demanding. As demonstrated, the proposed strategies achieve substantial time-to-solution improvements over existing state-of-the-art baselines and excellent scalability on multinode GPU architectures, with HPC innovations broadly applicable to the wider computational chemistry and materials science communities.

II. BACKGROUND

A. NC-SOC-DFT Governing Equations

Incorporating noncollinear magnetism into DFT requires representing single-electron wavefunctions as 2-component complex spinors [19], [20]

$$\Psi_n(\mathbf{r}) = \begin{pmatrix} \psi_n^\uparrow(\mathbf{r}) \\ \psi_n^\downarrow(\mathbf{r}) \end{pmatrix} \quad \forall n = 1, \dots, N_e, \quad (1)$$

where N_e is the number of electrons. The electron charge density $\rho(\mathbf{r})$ and the magnetization density $\mathbf{m}(\mathbf{r})$ are given by

$$\rho(\mathbf{r}) = \sum_n f_n \Psi_n^\dagger(\mathbf{r}) \Psi_n(\mathbf{r}), \quad \mathbf{m}(\mathbf{r}) = \sum_n f_n \Psi_n^\dagger(\mathbf{r}) \vec{\sigma} \Psi_n(\mathbf{r}), \quad (2)$$

where f_n are the Fermi occupations, \dagger denotes the complex-conjugate transpose, and $\vec{\sigma} = \sigma_x \hat{x} + \sigma_y \hat{y} + \sigma_z \hat{z}$ is the Pauli vector. The Kohn-Sham (KS) equations then take the form of a nonlinear Hermitian eigenvalue problem [9], [19]

$$H \Psi_n = \epsilon_n \Psi_n, \quad (3)$$

to be solved for the N_e spinors corresponding to the N_e smallest eigenvalues. The Hamiltonian operator can be decomposed as $H = H_{\text{loc}} + H_{\text{nlloc}}$, where the local part is

$$H_{\text{loc}} = \left(-\frac{1}{2}\nabla^2 + V_{\text{eff}}(\mathbf{r})\right) \mathbf{I} + \mathbf{B}_{\text{xc}} \cdot \vec{\sigma}, \quad (4)$$

with \mathbf{I} the 2×2 identity matrix. The effective potential and exchange-correlation magnetic field are

$$V_{\text{eff}} = V_{\text{el}} + V_{\text{xc}} + (V_{\text{loc}} - V_{\text{self}}), \quad V_{\text{xc}} = \frac{\delta E_{\text{xc}}}{\delta \rho}, \quad \mathbf{B}_{\text{xc}} = \frac{\delta E_{\text{xc}}}{\delta \mathbf{m}}. \quad (5)$$

The total electrostatic potential V_{el} and the nuclear self-interaction potential V_{self}^a are solutions of the Poisson problems [18], [21]

$$-\nabla^2 V_{\text{el}}(\mathbf{r}) = 4\pi(\rho(\mathbf{r}) + b(\mathbf{r}, \mathbf{R})), \quad (6)$$

$$-\nabla^2 V_{\text{self}}^a(\mathbf{r}, \mathbf{R}_a) = 4\pi b^a(\mathbf{r} - \mathbf{R}_a), \quad (7)$$

where $b(\mathbf{r}, \mathbf{R}) = \sum_a b^a(\mathbf{r} - \mathbf{R}_a)$ is the total smeared nuclear charge density. The non-local part H_{nlloc} encodes the spin-orbit interaction via the separable optimized norm-conserving Vanderbilt (ONCV) pseudopotential [22], [23] and acts on a spinor as

$$H_{\text{nlloc}} \Psi_n(\mathbf{r}) = \int V_{\text{nlloc}}(\mathbf{r}, \mathbf{r}') \Psi_n(\mathbf{r}') d\mathbf{r}', \quad (8)$$

where $V_{\text{nlloc}}(\mathbf{r}, \mathbf{r}')$ is the non-local pseudopotential kernel whose 2×2 matrix structure in spin space captures the full relativistic coupling between spin-orbit split angular-momentum channels. We note that Equation (3) is a nonlinear eigenvalue problem and solved as a sequence of linear eigenproblems using a self-consistent field (SCF) iteration.

B. State of the Art

Solving the KS eigenproblem in practice requires a suitable discretization of the governing equations. The most widely used approach in solid-state calculations is the plane-wave (PW) basis [24], [25], which enjoys spectral convergence but suffers from well-known limitations: poor scalability on massively parallel architectures and inability to handle non-periodic systems efficiently. Real-space discretization methods — based on finite differences [26], [27], wavelets [28], and finite elements [29]–[31] — have emerged as scalable alternatives that accommodate generic boundary conditions and are amenable to adaptive resolution.

Among these, the finite-element (FE) basis, built from compactly supported, piecewise-polynomial functions constructed on an adaptively refined mesh, offers a particularly compelling combination of properties for large-scale DFT on modern heterogeneous architectures. The locality of FE basis functions gives rise to sparse discretized operators whose action can be evaluated locally at FE cell level, enabling fine-grained parallelism [32]–[34] and efficient GPU utilization through dense batched matrix-matrix products [18]. The open-source DFT-FE code [18], [21] exploits these features and has demonstrated exceptional scalability for collinear-spin DFT, handling systems with up to 100,000 electrons on 200,000 CPU cores and 40,000 GPUs.

C. Computational Challenges at Scale

Extending DFT to incorporate noncollinear magnetism and SOC introduces a qualitatively different computational regime. The use of 2-component complex spinors doubles the dimension of the FE-discretized Hamiltonian from M to $2M$ (where M is the number of FE grid points), and the number of eigenpairs to be computed increases from $N_e/2$ (collinear) to N_e (non-collinear), all in complex arithmetic. Complex floating-point operations carry a higher cost ($\approx 3\times$ to $4\times$) than their real counterparts, and together these factors increase the computational prefactor by approximately $12\times$ – $24\times$ relative to standard collinear DFT calculations depending on the sizes of the material systems studied. To this end, excepting very few recent works [35], [36], routine NC-SOC-DFT calculations with state-of-the-art DFT codes are confined to systems of ~ 500 – 2000 electrons. Reaching the $\mathcal{O}(10^4)$ – $\mathcal{O}(10^5)$ electron regime in a scalable manner is computationally very challenging and prior DFT calculations reaching scales of $\mathcal{O}(10^5)$ electrons were limited to collinear-spin formulations [1]–[7]. Addressing this computational challenge demands co-designed algorithmic and HPC innovations targeting the computationally dominant steps of the SCF algorithm: the linear solver for DFT electrostatics (Eqn. (6)) and the eigensolver for the Kohn-Sham DFT eigenproblem (Eqn. (3)) and is the focus of the current work.

III. INNOVATIONS REALIZED

The NC-SOC-DFT equations described in Section II are solved by combining a higher-order adaptive finite-element (FE) discretization with efficient solver strategies and GPU-centric HPC innovations. We first describe the FE discretization and its challenges specific to NC-SOC, followed by the solver strategies and HPC innovations that enable large-scale calculations.

A. Finite-element discretization for NC-SOC-DFT

The 2-component complex spinors in the FE basis are expressed as

$$\Psi_n(\mathbf{r}) = \sum_{I=0}^{M-1} \begin{bmatrix} \psi_n^{I,\uparrow} \\ \psi_n^{I,\downarrow} \end{bmatrix} N_I(\mathbf{r}), \quad (9)$$

where $N_I(\mathbf{r})$ are 3D tensor-structured FE polynomial basis functions constructed from 1D Lagrange polynomials of degree p on Gauss–Lobatto–Legendre (GLL) nodes, and M is the number of FE nodes. This discretization converts the KS eigenproblem (Equation (3)) into a $2M \times 2M$ sparse generalized Hermitian eigenvalue problem $\mathbf{H}\mathbf{X} = \mathbf{M}\mathbf{X}\Lambda$, where the Hamiltonian $\mathbf{H} = \mathbf{H}^{\text{loc}} + \mathbf{H}^{\text{nlloc}}$ and the overlap matrix \mathbf{M} are complex Hermitian matrices. The local part \mathbf{H}^{loc} encodes kinetic, effective potential, and exchange-correlation magnetic field (\mathbf{B}_{xc}) contributions, while $\mathbf{H}^{\text{nlloc}}$ encodes the spin-orbit coupling via the separable pseudopotential. The overlap matrix has the form $M_{2I+\alpha, 2J+\beta} = \delta_{\alpha\beta} \int N_I(\mathbf{r})N_J(\mathbf{r}) d\mathbf{r}$, which is diagonal in spin indices but couples different FE nodes.

All integrals are evaluated by decomposing them over non-overlapping hexahedral FE cells $\Omega^{(e)}$ using Gauss–Legendre quadrature rules of sufficiently high order [36]. Similarly, the total electrostatic potential V_{el} is obtained by solving the FE-discretized Poisson equation $\mathbf{K}V_{\text{el}} = \rho$, where \mathbf{K} is the discrete Laplacian operator.

a) Challenges specific to NC-SOC.: The NC-SOC discretization introduces several challenges beyond the collinear case. First, as stated before, the 2-component spinor structure doubles the problem dimension from M to $2M$ and requires complex arithmetic throughout, increasing the computational cost by approximately $12\times$ – $24\times$. Second, evaluation of the exchange-correlation magnetic field \mathbf{B}_{xc} for GGA functionals requires gradients of the magnetization unit vector $\hat{\mathbf{m}} = \mathbf{m}/|\mathbf{m}|$, which become singular when $|\mathbf{m}| \rightarrow 0$. The standard divergence-theorem approach used in collinear calculations [18], [21] to recast Laplacians as gradients fails in the NC case due to this singularity. We address this by extending the White–Bird formalism [36] to the FE setting, computing V_{xc} and \mathbf{B}_{xc} directly at quadrature points as functional derivatives of the discretized exchange-correlation energy with respect to ρ and $|\mathbf{m}|$, thereby avoiding the ill-defined gradient of $\hat{\mathbf{m}}$. Third, the non-local pseudopotential operator acquires a full 2×2 spin-block structure coupling the two spinor components through the SOC channels, requiring modified projection and assembly routines. The resulting discretized problem is solved via a self-consistent field (SCF) iteration using Anderson mixing with Resta-like preconditioning [37], where each SCF step requires: (i) solving the Poisson equation for V_{el} , (ii) evaluating V_{xc} and \mathbf{B}_{xc} , and (iii) solving the $2M \times 2M$ generalized eigenproblem for N_e eigenpairs. The efficient solution of steps (i) and (iii) — the computational bottlenecks at scale — is described next.

B. Efficient and scalable solver strategies

1) Linear solver for electrostatic problem.: The FE-discretized Poisson problems (Equation (6)) are solved with a preconditioned conjugate gradient (PCG) method, where the dominant cost per iteration is the application of the discrete Laplace operator \mathbf{K} to a trial vector. We implement this matrix-vector product as a matrix-free GPU kernel that exploits the tensor-product structure of the FE basis. Since d -dimensional basis functions factor into products of 1D shape functions,

the stiffness matrix action decomposes into a sequence of 1D contractions, reducing the per-element cost from $\mathcal{O}(p^{2d})$ to $\mathcal{O}(dp^{d+1})$ for polynomial order p . The full sequence (extraction, contractions, Jacobian application, and assembly) is fused into a single GPU kernel, keeping all intermediate data in registers or shared memory. The 1D shape function and gradient arrays are stored in shared memory for hardware-managed broadcast, and intermediate values that require no inter-thread communication are held in registers to reduce shared memory pressure and increase occupancy.

For preconditioning, we employ a Chebyshev polynomial expansion of the inverse of the discrete Laplace operator. The Chebyshev recurrence requires repeated application of \mathbf{K} and a diagonal scaling, both of which are performed using the same matrix-free infrastructure described.

2) *Residual-based Chebyshev filtered subspace iteration:* The FE-discretized KS eigenproblem (Equation (3)) yields a sparse generalized Hermitian eigenvalue problem

$$\mathbf{H}\mathbf{x}_j = \epsilon_j \mathbf{M}\mathbf{x}_j, \quad j = 1, \dots, N_e, \quad (10)$$

where $\mathbf{H} \in \mathbb{C}^{2M \times 2M}$ is the discretized Hamiltonian, $\mathbf{M} \in \mathbb{C}^{2M \times 2M}$ is the FE overlap (mass) matrix, and $2M$ is twice the number of FE nodes. In previous collinear DFT-FE implementations [5], [21], \mathbf{M} was rendered diagonal via a spectral FE or lumped-mass approximation, thereby reducing Equation (10) to a standard eigenproblem. In the NC-SOC setting, however, the off-diagonal 2×2 spin-block structure of the discretized operators makes a diagonal approximation of \mathbf{M} infeasible without sacrificing accuracy, and one must solve the full generalized eigenproblem.

We solve Equation (10) with Chebyshev filtered subspace iteration (ChFSI) [38], which constructs a filtered subspace $\mathbf{Y}_p^{(i)} = C_p(\mathbf{M}^{-1}\mathbf{H})\mathbf{X}^{(i)}$ via the three-term Chebyshev recurrence

$$\mathbf{Y}_{k+1}^{(i)} = \frac{2\sigma_{k+1}}{e} \mathbf{M}^{-1} \mathbf{H} \mathbf{Y}_k^{(i)} - \frac{2\sigma_{k+1}c}{e} \mathbf{Y}_k^{(i)} - \sigma_k \sigma_{k+1} \mathbf{Y}_{k-1}^{(i)}, \quad (11)$$

where c and e are the center and half-width of the unwanted spectrum, and σ_k are damping coefficients. Each recurrence step requires a sparse matrix–multivector product followed by the action of \mathbf{M}^{-1} . Computing the exact inverse \mathbf{M}^{-1} is prohibitively expensive for large-scale problems; in practice one substitutes a cheap approximation $D^{-1} \approx \mathbf{M}^{-1}$ (e.g. the inverse of the diagonal of \mathbf{M}). However, the resulting approximation error $\Delta_p^{(i)} = \underline{\mathbf{Y}}_p^{(i)} - \mathbf{Y}_p^{(i)}$ in the filtered subspace remains bounded by a constant independent of the eigenproblem residual [39], causing ChFSI to stagnate at a residual floor determined by the approximation quality rather than converging to the desired tolerance. This limitation is particularly relevant in the NC-SOC setting, where the non-collinear magnetization density is sensitive to the diagonal approximation of \mathbf{M} , necessitating the use of the full mass matrix and consequently an approximate inverse $D^{-1} \approx \mathbf{M}^{-1}$ in the Chebyshev recurrence.

a) *Residual-based reformulation (R-ChFSI):* To overcome this limitation, we employ the residual-based ChFSI (R-ChFSI) method [39], which reformulates the Chebyshev recurrence in terms of weighted residuals $\mathbf{Z}_k^{(i)} = D(\mathbf{Y}_k^{(i)} - \mathbf{X}^{(i)} C_k(\Lambda^{(i)}))$, where $\Lambda^{(i)}$ contains the current eigenvalue estimates. As the eigenpairs converge, these residuals approach zero, so any error introduced by low-precision arithmetic or by using D^{-1} in place of \mathbf{M}^{-1} translates into an absolute error proportional to the residual norm $\|\mathbf{R}^{(i)}\|$, which itself decreases with each SCF iteration. The R-ChFSI recurrence replaces Equation (11) with

$$\mathbf{Z}_{k+1}^{(i)} = \frac{2\sigma_{k+1}}{e} \mathbf{H} D^{-1} \mathbf{Z}_k^{(i)} - \frac{2\sigma_{k+1}c}{e} \mathbf{Z}_k^{(i)} - \sigma_k \sigma_{k+1} \mathbf{Z}_{k-1}^{(i)} + \frac{2\sigma_{k+1}}{e} \mathbf{M} \mathbf{R}^{(i)} \Lambda_k^{(i)}, \quad (12)$$

where $\mathbf{R}^{(i)} = \mathbf{H}\mathbf{X}^{(i)} - \mathbf{M}\mathbf{X}^{(i)}\Lambda^{(i)}$ is the eigenproblem residual computed once per SCF step in double precision, and $\Lambda_k^{(i)} = C_k(\Lambda^{(i)})$ is propagated via a scalar recurrence. After p steps, the filtered vectors are recovered as $\mathbf{Y}_p^{(i)} = D^{-1} \mathbf{Z}_p^{(i)} + \mathbf{X}^{(i)} \Lambda_p^{(i)}$. This reformulation is critical for the NC-SOC eigenproblem: it permits the use of a simple diagonal D^{-1} for the full non-diagonal mass matrix \mathbf{M} while still converging to double-precision accuracy. The overall R-ChFSI eigensolver procedure is summarized in Algorithm 1.

Algorithm 1 R-ChFSI eigensolver for the generalized Hermitian eigenproblem

Require: $\mathbf{H}, \mathbf{M} \in \mathbb{C}^{2M \times 2M}$; number of eigenpairs N_e ; polynomial degree p ; spectral bounds $\lambda_{\min}, \lambda_{\max}, \lambda_T$; diagonal preconditioner $D^{-1} \approx \mathbf{M}^{-1}$; tolerance τ

Ensure: Eigenvectors $\mathbf{X}^{(i+1)} \in \mathbb{C}^{2M \times N_e}$, eigenvalues $\Lambda^{(i+1)}$

- 1: Choose initial guess $\mathbf{X}^{(0)}$; set $i \leftarrow 0$
 - 2: **while** $\max_j \|\mathbf{H}\mathbf{x}_j^{(i)} - \epsilon_j^{(i)} \mathbf{M}\mathbf{x}_j^{(i)}\| \geq \tau$ **do**
 - 3: Compute residual $\mathbf{R}^{(i)} = \mathbf{H}\mathbf{X}^{(i)} - \mathbf{M}\mathbf{X}^{(i)}\Lambda^{(i)}$ ▷
 - 4: **R-ChFSI filter:** Compute $\mathbf{Z}_p^{(i)}$ via Equation (12) ▷
 - 5: low precision mat-vecs (FP32 or TF32)
 - 6: Recover $\mathbf{Y}_p^{(i)} = D^{-1} \mathbf{Z}_p^{(i)} + \mathbf{X}^{(i)} \Lambda_p^{(i)}$
 - 7: **Rayleigh–Ritz (RR) step:**
 - 8: Solve subspace eigenproblem:
 - 9: $\mathbf{Y}_p^{(i)\dagger} \mathbf{H} \mathbf{Y}_p^{(i)} \mathbf{Q} = \mathbf{Y}_p^{(i)\dagger} \mathbf{M} \mathbf{Y}_p^{(i)} \mathbf{Q} \Lambda^{(i+1)}$
 - 10: Subspace rotation (SR): $\mathbf{X}^{(i+1)} \leftarrow \mathbf{Y}_p^{(i)} \mathbf{Q}$
 - 11: $i \leftarrow i + 1$
 - 12: **end while**
-

R-ChFSI enables the two key performance innovations in this work. First, the matrix–multivector products in Equation (12) can be evaluated in single precision (FP32), since the residual-proportional error bound [39] ensures that the reduced-precision errors do not impede convergence. Second, the P2P communication of the filtered residual vectors $\mathbf{Z}_k^{(i)}$ during the sparse mat-vecs can be compressed using block floating-point (BFP) at compression ratios exceeding $4\times$,

further reducing data movement costs. Both strategies are detailed in the subsequent sections.

C. HPC Innovations

1) GPU-Accelerated Matrix-Free Conjugate Gradient Solver: Algorithmic and Kernel-Level Optimizations:

a) *Overview of the CG Solver:* Our GPU-accelerated conjugate gradient (CG) solver keeps all vector operations, inner products, and matrix-vector products on the GPU throughout the iteration. We minimize global memory traffic and MPI collectives by fusing the two inner products $\mathbf{r} \cdot \mathbf{z}$ and $\mathbf{r} \cdot \mathbf{r}$ into a single device kernel, and by fusing the updates to \mathbf{x} and \mathbf{r} with $\|\mathbf{r}\|^2$ accumulation, yielding exactly two MPI_Allreduce calls per iteration regardless of problem size (Algorithm 2).

Algorithm 2 GPU-Accelerated Preconditioned CG Iteration (Fused Kernels)

Require: \mathbf{x} , \mathbf{r} , \mathbf{p} , \mathbf{z} , δ (from previous iteration or initialization)

Ensure: Updated \mathbf{x} , \mathbf{r} , $\delta_{\text{new}} = \mathbf{r} \cdot \mathbf{z}$

- 1: **Kx kernel:** $\mathbf{w} \leftarrow \mathbf{K}\mathbf{p}$ \triangleright extract \rightarrow Z/Y/X contractions (even/odd sym.), Jacobian in regs., fused D^T + assemble
- 2: **Dot kernel:** $\sigma \leftarrow \mathbf{p} \cdot \mathbf{w}$ [5-phase: regs \rightarrow warp-shfl \rightarrow smem \rightarrow block \rightarrow atomic]
- 3: MPI_Allreduce (σ , 1 scalar) \triangleright global $\mathbf{p} \cdot \mathbf{w}$
- 4: $\alpha \leftarrow \delta / \sigma$
- 5: **Fused update kernel:** $\mathbf{x} += \alpha\mathbf{p}$; $\mathbf{r} += \alpha\mathbf{w}$; $\gamma \leftarrow \|\mathbf{r}\|^2$ \triangleright single pass; $\|\mathbf{r}\|^2$ accumulated in registers
- 6: **Chebyshev precond.:** $\mathbf{z} \leftarrow \mathbf{P}^{-1}\mathbf{r}$ \triangleright fused residual + update + accumulate
- 7: **Fused dot kernel:** $(\delta_{\text{new}}, \gamma) \leftarrow (\mathbf{r} \cdot \mathbf{z}, \|\mathbf{r}\|^2)$ \triangleright single pass, 2 register accumulators \Rightarrow 2 scalars
- 8: MPI_Allreduce ($[\delta_{\text{new}}, \gamma]$, 2 scalars) \triangleright global $\mathbf{r} \cdot \mathbf{z}$ and $\|\mathbf{r}\|^2$
- 9: $\beta \leftarrow \delta_{\text{new}} / \delta$; $\delta \leftarrow \delta_{\text{new}}$
- 10: $\mathbf{p} \leftarrow -\mathbf{z} + \beta\mathbf{p}$
- 11: **if** $\sqrt{\gamma} < \varepsilon$ **then** converged **end if**

b) *The Kx Kernel: Fusing Extraction, Tensor Contractions, and Assembly:* The most computationally intensive component is the matrix-free action of the operator \mathbf{K} , which applies the finite-element stiffness matrix without explicitly forming it [34]. This kernel is implemented as a sequence of six batched tensor contractions corresponding to: (i) interpolation of nodal values to quadrature points, (ii) application of the Jacobian-transformed metric tensor, and (iii) integration back to the nodal basis, all within a single device kernel launch. It uses a register-shared memory hybrid: intermediate contraction outputs stay in registers until inter-thread communication requires staging through shared memory.

- *Combining Extraction with the First Tensor Contraction:* The z -direction contraction is fused with data extraction: each thread reads a column from global memory and immediately accumulates the contraction into a private register array, overlapping memory latency with arithmetic. This is especially effective at higher polynomial

orders where the workload is memory-bound. Once the z -direction pass is complete, results are written to shared memory and a sync barrier is issued. Subsequent y - and x -contractions read from shared memory and exploit even/odd symmetry to halve the operation count.

- *Hybrid Register-Shared Memory Strategy:* Intermediate results that require no inter-thread communication are kept in registers; only values that must be visible to other threads are written to shared memory at synchronization boundaries. The gradient contractions and the Jacobian is applied entirely in registers, reducing shared memory pressure and increasing occupancy.
- *Combining the Last Contraction with the Assembly Step:* The final contraction back to the nodal basis is fused with the assembly step: output values produced in registers are accumulated directly into the output array via atomic additions, without an intermediate staging step, eliminating one full global memory pass.

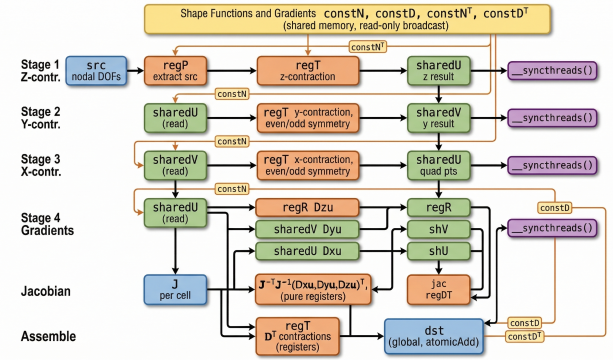


Fig. 1: Hybrid register-shared memory strategy in the matrix-free Kx kernel. Intermediate contraction outputs that require no inter-thread communication are kept in registers; only values needed by other threads are staged through shared memory at synchronization boundaries.

c) *Preconditioner Optimizations:* The Chebyshev polynomial preconditioner operates on a diagonal approximation $\mathbf{P} \approx \text{diag}(\mathbf{K})$. The initialization kernel computes action of \mathbf{P}^{-1} in registers and then each subsequent Chebyshev step fuses the residual computation, the direction rescaling, and the output accumulation into a single kernel, keeping all intermediates in registers.

d) *Dot Product Kernels: Five-Phase Tree Reduction:* The inner product kernels exploit the GPU memory hierarchy through a five-phase tree reduction. In Phase 1, each thread accumulates a partial sum directly into registers (two accumulators for the fused $\mathbf{r} \cdot \mathbf{z}$ and $\mathbf{r} \cdot \mathbf{r}$ kernel). In Phase 2, a warp-level reduction is performed via shuffle intrinsics, leaving the per-warp partial sum in the lane-0 register without accessing shared memory.

In Phases 3–5, the lane-0 thread of each warp writes its result to shared memory; a second tree reduction with sync barrier collapses to a single block-level partial sum; and thread 0 of each block issues 2 atomic additions to the pre-zeroed global accumulators. The bulk of the floating-point work thus stays in registers and first-level caches, with

only 2 global atomics per threadblock at the end. The fused two-output variant halves kernel launch overhead and global memory traffic compared to two separate dotproduct kernels.

2) *Reduced precision arithmetic for mat-multivecs in R-ChFSI*: The dominant cost of each R-ChFSI iteration is the sparse Hamiltonian–multivector product $\mathbf{H}\mathbf{X}$. A direct sparse-matrix times dense-matrix (spMM) kernel is memory-bandwidth bound and achieves poor utilization on modern GPUs. We instead exploit the compact support of the FE basis to recast the global spMM into batched cell-level dense matrix–matrix products [34], [36] that are compute-bound and map directly onto high-throughput GEMM hardware units. Each FE cell $\Omega^{(e)}$ carries a precomputed dense local Hamiltonian $\mathbf{H}^{\text{loc}(e)}$ of size $2n_p^3 \times 2n_p^3$, where $n_p = p + 1$ is the number of GLL nodes per direction and the factor of 2 accounts for the spinor components. In the NC-SOC case, the 2×2 spin-block structure is

$$\mathbf{H}^{\text{loc}(e)} = \begin{bmatrix} \mathbf{H}_{\text{scal}}^{(e)} + \mathbf{H}_{B_z}^{(e)} & \mathbf{H}_{B_x}^{(e)} - i\mathbf{H}_{B_y}^{(e)} \\ \mathbf{H}_{B_x}^{(e)} + i\mathbf{H}_{B_y}^{(e)} & \mathbf{H}_{\text{scal}}^{(e)} - \mathbf{H}_{B_z}^{(e)} \end{bmatrix}, \quad (13)$$

where $\mathbf{H}_{\text{scal}}^{(e)}$ encodes the kinetic and effective potential contributions and $\mathbf{H}_{B_d}^{(e)}$ ($d = x, y, z$) encode the exchange-correlation magnetic field components. The product $\mathbf{Y} = \mathbf{H}\mathbf{X}$ is evaluated in four stages: (i) cell-level multivector extraction $\mathbf{X}^{(e)} = \mathcal{R}^{(e)}\mathbf{X}$ via index-gather into contiguous GPU buffers; (ii) batched strided GEMM over all local cells, $\mathbf{Y}^{(e)} = \mathbf{H}^{\text{loc}(e)}\mathbf{X}^{(e)}$, where each batch element is a $(2n_p^3) \times (2n_p^3) \times (2n_p^3) \times N_b$ product with N_b wavefunctions; (iii) assembly via index-scatter with atomic additions $\mathbf{Y} += \mathcal{R}^{(e)T}\mathbf{Y}^{(e)}$; and (iv) non-local pseudopotential contributions computed through cell-level projector matrices $\mathbf{P}^{a(e)}$ and the SOC coefficient matrices Δ^{γ_a} , similarly evaluated as batched GEMMs. The extraction–GEMM–assembly pipeline is overlapped with nearest-neighbour MPI halo exchange (scatter/gather of ghost values) for the domain-decomposed FE mesh, hiding communication latency behind the compute-intensive cell GEMMs.

This cell-matrix formulation directly enables mixed-precision computation in the R-ChFSI filtering step. After the FP64 assembly of $\mathbf{H}^{\text{loc}(e)}$, FP32 copies are generated via a single device-to-device cast at negligible cost. During R-ChFSI filtering, all batched GEMMs—which constitute the bulk of the FLOP count—execute in FP32, and on architectures with dedicated matrix engines (e.g. Intel PVC), the GEMM calls further leverage TF32 tensor operations via the oneMKL interface for additional acceleration. The extraction, scatter/gather, and assembly kernels similarly operate on FP32 multivectors, halving global memory traffic relative to FP64. Only the eigenproblem residual $\mathbf{R}^{(i)}$ and the eigenvalue recurrence $\Lambda_k^{(i)}$ are retained in FP64, ensuring that the R-ChFSI convergence bound holds and the overall solver delivers double-precision accuracy.

3) *Block floating point compression for domain decomposition communication*: In a finite element (FE) discretization, the basis functions are locally supported, so point-to-point

(P2P) communication is restricted to nearest neighbors across processor boundaries. Each Chebyshev filtering pass consists of two halo phases: a scatter phase, in which each rank sends its locally owned boundary entries to neighboring ghost holders, and a gather phase, which returns the accumulated ghost contributions to the owning rank’s local data (Fig. 2). The amount of data exchanged per pass is $n_{\text{boundary}} \times N_b$ values; thus, the communication volume is directly proportional to the number of bits per value (bpv) used to represent the data (e.g., 32 for FP32 precision).

As the system size increases and more computational nodes are employed, the Chebyshev filtering phase becomes the dominant cost. Residual-based Chebyshev filtering [39], which is tolerant to inexact matrix–vector products, enables the use of FP32 precision (with TF32 GEMMs) for computation and FP32 for communication, accelerating the filtering phase by nearly a factor of $2 \times$. Furthermore, using BF16 precision for communication alone yields additional performance gains of up to $1.5 \times$ without degrading convergence for most systems. However, for systems with harder pseudopotentials, BF16 communication can increase the number of required SCF iterations, offsetting the benefits of reduced-precision communication.

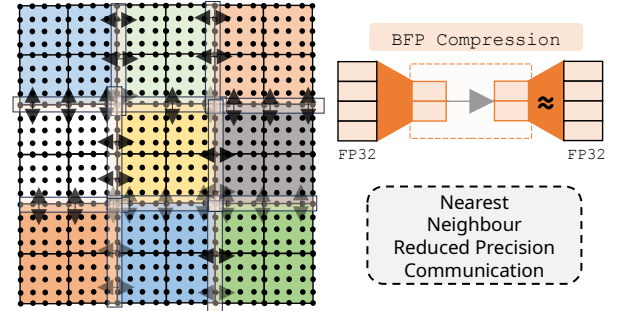


Fig. 2: Domain decomposition of the simulation domain, where each color denotes a distinct MPI rank. Arrows denote P2P nearest-neighbour communication across partition boundaries: ghost values, originally in FP32, are compressed on the sending GPU to a chosen bits-per-value rate, transmitted as a fixed-size byte stream, and decompressed on the receiving GPU.

To this end, we adopt a block floating-point (BFP) representation to compress ghost boundary values at a predetermined fixed rate, with near-zero compression and decompression overhead, reducing communication costs while preserving convergence. BFP assigns a common exponent — determined by the largest absolute value in the block — to a group of four consecutive FP32 values, which are then encoded as signed fraction bits under a fixed memory budget. Our lightweight BFP compression maps four FP32 values into a fixed-width payload of $m_{\text{bits}} = 4 \times \text{bpv}$ bits. The lower 8 bits store a shared biased exponent spanning the full FP32 dynamic range; the remaining bits are divided equally among four signed two’s-complement coefficients of

$$v_{\text{bits}} = \frac{m_{\text{bits}} - 8}{4}$$

bits each (Fig. 3). For the rates used here, this yields $v_{\text{bits}} = 14, 10, 8, 6$ for $\text{bpv} = 16, 12, 10, 8$, respectively. At 16 bpv,

each value retains 14 signed fractional bits—nearly twice the BF16 mantissa width—while still achieving a $2\times$ compression ratio relative to FP32.

The shared exponent e_{\max} satisfies $2^{e_{\max}-1} \leq \max_i |x_i| < 2^{e_{\max}}$; blocks below the representable precision floor are set to zero. Otherwise, the biased exponent $e = e_{\max} + 127$ is stored, and each value is quantised as

$$q_i = \text{round}(x_i \cdot 2^{v_{\text{bits}}-1-e_{\max}}), \quad q_i \in [-2^{v_{\text{bits}}-1}, 2^{v_{\text{bits}}-1}-1].$$

Decoding recovers $e_{\max} = e - 127$ and reconstructs

$$\tilde{x}_i = q_i \cdot 2^{e_{\max}-v_{\text{bits}}+1}.$$

Thus, encode performs compression and quantisation, while decode reconstructs from the stored bit fields; all approximation is introduced at encode time. Round-to-nearest avoids the systematic bias of truncation. Since residual boundary values typically have similar magnitudes and trend toward zero, the shared-exponent assumption is tight. Unlike ZFP [40], which applies decorrelation transforms and negabinary conversions to handle high-variability data—incurring higher arithmetic cost and potential thread divergence on GPUs—this vanilla BFP encoder has near-zero overhead. Compression techniques remain uncommon in scientific computing, particularly in electronic structure calculations where stringent accuracy requirements limit their use; their adoption here is enabled by the robustness of RChFSI.

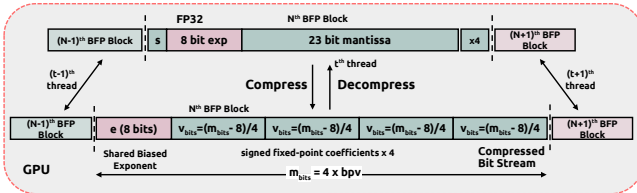


Fig. 3: Compression is performed at the granularity of one 4-value FP32 block per thread. Each block is packed into $m_{\text{bits}} = 4 \times \text{bpv}$ bits: one shared biased exponent (8 bits) and four signed $v_{\text{bits}} = (m_{\text{bits}} - 8)/4$ -bit coefficients. The compressed stream is laid out contiguously in thread/rank order with fixed-size slices, enabling exact byte offsets and atomic-free writes for the common rates $\text{bpv} \in \{16, 12, 10, 8\}$.

Each GPU thread encodes one 4-value block, providing maximum parallelism and producing exactly $4 \times \text{bpv}$ bits per block. For the common rates $\text{bpv} \in \{16, 12, 10, 8\}$, the layout ensures that each thread writes to a private output region, eliminating shared words and avoiding atomics. At 8 and 16 bpv, a block fits in a single `uint32_t` or `uint64_t` store, enabling fully coalesced writes. At 10 and 12 bpv, a block maps to $5 \times \text{uint8}_t$ or $3 \times \text{uint16}_t$ stores; these are less coalesced but remain conflict-free and atomic-free. In contrast to ZFP, which uses fixed 64-bit packing that can cause neighboring blocks to share a word and require atomic updates, our design avoids such conflicts. For other rates, a super-block layout is used: one thread processes multiple blocks such that the total output aligns with a 64-bit boundary, preserving atomic-free writes.

Boundary exchanges communicate residual values between owning and neighboring ranks. To reduce communication

bandwidth, a `compress` mode applies BFP compression and decompression during communication. On the send side, gathering and compression are combined in a single pass, so values are read once and written directly to the compressed buffer before `MPI_Isend`. On the receive side, the stream is decoded, and values are accumulated and scattered to the target entries in a single pass. In both cases, the GPU processes the entire buffer in a single pass, with no on-the-fly memory allocation or additional kernel launches. Thus, data movement and compression are performed together, with near-zero overheads.

Fixed-rate compression enables exact buffer slicing. If rank i exchanges n_i boundary entries with block size N_b , the message size is $n_i N_b \text{bpv}/8$ bytes. The compressed stream is stored contiguously in rank order, so the offset for rank i is the prefix sum of preceding slice sizes, with no padding between neighbors. This makes pointer advancement deterministic and avoids extra packing. A single device buffer is allocated at the maximum supported compressed size and reused. When `bpv` is reduced at runtime, only the active bytes are transferred before MPI, rounded up to an 8-byte boundary for alignment; thus, both device-to-host traffic and network volume shrink automatically without reallocating memory.

4) *Rayleigh-Ritz step*: The computational bottleneck in Algorithm 1 is the Rayleigh Ritz (RR) procedure with a computational cost that scales cubic with system. The RR procedure involves 3 critical steps: (i) `RR-Proj`: Projecting the FE-discretized Hamiltonian (\mathbf{H}) and overlap matrices (\mathbf{M}) onto the Chebyshev filtered space. (ii) `RR-diag`: Solving the generalised eigenvalue problem in the subspace. (iii) `RR-SR`: A subspace rotation procedure to get the eigenvectors. Among these steps, the `RR-Proj` and `RR-SR` steps are dominated by dense matrix-matrix multiplications and are implemented using Level-3 BLAS (e.g., GEMM) kernels. These operations are compute-intensive and exhibit high arithmetic intensity, making them well-suited for efficient execution on modern GPU architectures.

To improve scalability and reduce memory overhead, we employ a blockwise formulation of the RR procedure. In particular, the projection and subspace rotation operations are carried out in blocks of wavefunctions, thereby limiting peak memory usage and enabling better cache and device memory utilization. Furthermore, this blockwise strategy facilitates overlapping communication with computation by pipelining data movement with GEMM operations. Additionally, in the `RR-SR` step, the subspace rotation $\mathbf{Y}_p \mathbf{Q}$ is decomposed as

$$\mathbf{Y}_p \mathbf{Q} = \mathbf{Y}_p \mathbf{Q}_{\text{diag}} + \mathbf{Y}_p \mathbf{Q}_{\text{non-diag}}$$

where \mathbf{Q}_{diag} and $\mathbf{Q}_{\text{non-diag}}$ denote the diagonal and off-diagonal components of \mathbf{Q} , respectively. A mixed-precision strategy is employed wherein $\mathbf{Y}_p \mathbf{Q}_{\text{non-diag}}$ is evaluated in FP32 arithmetic, while $\mathbf{Y}_p \mathbf{Q}_{\text{diag}}$ is computed in FP64 arithmetic. The strategies discussed here reduce the computational pre-factor associated with the cubic-scaling Rayleigh-Ritz procedure.

5) *Band-partitioning approach*: Strong scaling (fixed-problem size) with the existing approach leads to increasing communication overhead during the Chebyshev filtering step as the degrees of freedom per GPU (DoFs/GPU) decrease. The overlap of computation and communication does not sufficiently mitigate this bottleneck, and the overall throughput remains limited by the slowest link latency/bandwidth. Crucially, however, the reduction in DoFs/GPU that accompanies strong scaling also results in a corresponding increase in free memory per GPU. The band-partitioning strategy exploits this available memory to reduce or eliminate the communication overhead during the filtering step beyond a group of GPUs.

Band-partitioning: 2D Process Grid

P(1,1)	P(1,2)	P(1,3)	P(1,4)	P(1,5)
P(2,1)	P(2,2)	P(2,3)	P(2,4)	P(2,5)
P(3,1)	P(3,2)	P(3,3)	P(3,4)	P(3,5)
P(4,1)	P(4,2)	P(4,3)	P(4,4)	P(4,5)

Fig. 4: Band-partitioning of 20 processing elements (GPUs) into 2D process grid with $n_c = 5$ column groups and $n_r = 4$ row groups.

The central idea is to replicate the Hamiltonian and overlap matrices, \mathbf{H} and \mathbf{M} , across discrete groups of GPUs. To this end, the available GPUs are arranged in a 2D process grid of n_r rows and n_c columns, where all GPUs within the same column constitute a column group. Figure 4 illustrates such an arrangement with $n_c = 5$ column groups and $n_r = 4$ row groups. Each column group maintains its own distributed copy of $\mathbf{H}, \mathbf{M} \in \mathbb{C}^{2M \times 2M}$. The trial multi-vectors $\mathbf{X} \in \mathbb{C}^{2M \times N_e}$ are partitioned column-wise across column groups, with each group’s share further distributed row-wise among its n_r constituent GPUs. Each column group therefore operates on an independent subset of the columns of \mathbf{X} and evaluates the corresponding matrix-multivector products entirely within the group, eliminating all inter-group communication during the filtering step. This replication is feasible because the matrices, \mathbf{H} and \mathbf{M} , being highly sparse, occupy significantly less memory per GPU than the dense trial multi-vectors; at extreme scaling, the per-GPU memory footprint of \mathbf{X} also becomes small. In the limiting case of $n_r = 1$ (one GPU per column group), the communication overhead during the filtering step is eliminated entirely, subject to sufficient memory being available per GPU.

The subsequent Rayleigh-Ritz (RR) step, by contrast, is performed optimally with a single column group ($n_c = 1$), corresponding to a 1D block row decomposition. The RR step involves evaluating projected quantities of the form $\mathbf{Y}_p^\dagger \mathbf{H} \mathbf{Y}_p$ and $\mathbf{Y}_p^\dagger \mathbf{M} \mathbf{Y}_p$, yielding $N_e \times N_e$ matrices that are small in practice since $M \gg N_e$. With $n_c > 1$, however, each column group holds only a subset of the columns of \mathbf{Y}_p , necessitating $\mathcal{O}(MN_e)$ inter-group communication overhead to assemble

the full projection – an overhead that grows with n_c . The band-partitioning approach therefore employs $n_c > 1$ during the filtering step, where intra-group communication can be hidden through computation-communication overlap, and reverts to $n_c = 1$ for the RR step, reconciling these two competing requirements.

Algorithm 3 The Rayleigh-Ritz (RR) step with band-partitioning strategy

Require: $\mathbf{Y}_p \in \mathbb{C}^{2M \times N_e}$ \triangleright Output of the filtering step
Require: $\mathbf{H}, \mathbf{M} \in \mathbb{C}^{2M \times 2M}$

- 1: $\mathbf{Z}_M \leftarrow \mathbf{M} \mathbf{Y}_p$
- 2: $\mathbf{Z}_H \leftarrow \mathbf{H} \mathbf{Y}_p$
 \triangleright Steps 3–4: 2D block \rightarrow 1D block row layout conversion
- 3: AlltoAll($\mathbf{Y}_p, \mathbf{Z}_M, \mathbf{Z}_H$) in Row Group
- 4: ConvertLayout($\mathbf{Y}_p, \mathbf{Z}_M, \mathbf{Z}_H$)
- 5: $\mathbf{X}, \mathbf{\Lambda} = \text{standard RR}(\mathbf{Y}_p, \mathbf{Z}_M, \mathbf{Z}_H)$
 \triangleright Steps 6–7: 1D block row \rightarrow 2D block layout conversion
- 6: ConvertLayout(\mathbf{X})
- 7: AlltoAll(\mathbf{X}) in Row Group
- 8: **return** $\mathbf{X}, \mathbf{\Lambda}$ \triangleright Output eigenvectors and eigenvalues

Algorithm 3 details the modified RR step under the band-partitioning strategy. At the start of each RR step, the data layout of trial multi-vectors is converted from the 2D block decomposition to the 1D block row decomposition via an AlltoAll collective among GPUs within the same row group, followed by a block-wise transpose (ConvertLayout). The standard RR substeps — RR-Proj, RR-diag, and RR-SR — are then executed with communication overhead no greater than that of the existing approach. Once complete, the inverse layout conversion is applied to restore the 2D block decomposition before the next ChFSI iteration begins. The optimal choice of n_c therefore reflects the trade-off between the communication savings in the filtering step and the additional AlltoAll overhead incurred during the layout conversions at each RR step.

Since AlltoAll and ConvertLayout are out-of-place operations, each layout conversion requires an additional memory buffer of the same size as \mathbf{X} (or \mathbf{Y}_p). Due to current implementation constraints, however, the overlap and the Hamiltonian matrix-multivector products ($\mathbf{M} \mathbf{Y}_p$ and $\mathbf{H} \mathbf{Y}_p$) each require separate buffers, increasing the total additional memory overhead for $4 \times$ the size of \mathbf{Y}_p . The total additional memory cost per GPU is therefore $4MN_e/n_p + (n_c - 1)\mathcal{M}_{\mathbf{H}, \mathbf{M}}$, where $n_p = n_r \times n_c$ is the total number of GPUs and $\mathcal{M}_{\mathbf{H}, \mathbf{M}}$ denotes the combined per-GPU memory footprint of \mathbf{H} and \mathbf{M} in the non-replicated ($n_c = 1$) case. The second term accounts for the $(n_c - 1)$ additional copies of \mathbf{H} and \mathbf{M} introduced by the band-partitioning replication.

As detailed in the Algorithm 3, each RR step requires $4 \times$ AlltoAll collectives under the band-partitioning strategy. In the standard $\alpha - \beta$ latency – bandwidth model, the corresponding AlltoAll communication cost per layout conversion is approximately $\alpha(n_c - 1) + \beta MN_e/n_p$. Both the memory

TABLE I: Benchmark systems used for performance evaluation. The degrees of freedom (DoFs) are twice the number of FE nodes due to the 2-component spinor structure in the NC-SOC formulation.

System	θ (deg)	Atoms	Val. e^-	DoFs/atom
FGT	7.3	732	11,468	$\sim 45k$
MoSe ₂	2.1	4,326	37,492	$\sim 16k$
MoSe ₂	1.5	9,114	78,988	$\sim 16k$

cost of trial multi-vectors and the bandwidth component of the communication cost scale as $\mathcal{O}(MN_e/n_p)$ and diminish as n_p increases, making band-partitioning strategy particularly effective at extreme scaling regimes.

IV. PERFORMANCE EVALUATION

We report our performance evaluation studies of our proposed strategies on representative benchmarks using ALCF exascale supercomputing system Aurora [41]

A. Systems and environment

The ALCF Aurora supercomputer comprises 10,624 compute nodes, each featuring two Intel Xeon CPU Max processors and six Intel Data Center GPU Max (Ponte Vecchio) GPUs with two Graphic Compute Dies (GCDs) in each GPU, for a total of 21,248 CPUs and 63,744 GPUs. Each node has 8 HPE Slingshot-11 NICs, and the system is connected in a Dragonfly topology. Information about the compiler and library versions can be found in the appendix.

B. Applications used to measure performance

We evaluate our framework on two scientifically important classes of twisted bilayer systems exhibiting noncollinear magnetism and spin-orbit coupling. The first is a twisted bilayer Fe₃GeTe₂ (FGT) system, a layered van der Waals ferromagnet that has attracted intense interest for its itinerant 2D ferromagnetism [42] and gate-tunable room-temperature magnetic order [43], making it a prime candidate for spintronic device applications. The second class consists of twisted bilayer MoSe₂ systems, heavy-element transition metal dichalcogenides where SOC-induced band splitting, spin-valley locking, and emergent Moiré physics [44], [45] necessitate large supercells for predictive simulations. The twisted bilayer structures were generated using the Twister code [46]. All calculations employ SG15 optimized norm-conserving Vanderbilt pseudopotentials [22], [47] within the PBE-GGA exchange-correlation functional [48]. The FE discretization uses adaptive meshes with polynomial order $p = 7$; for FGT, the mesh size near nuclei is 1.3 Bohr, and for MoSe₂ it is 2.1 Bohr. These meshes are chosen to achieve an accuracy of 10^{-4} Ha/atom, verified on smaller representative systems. The benchmark systems and their parameters are summarized in Table I.

C. Matrix-free GPU accelerated conjugate gradient solver

Figure 5 compares the throughput of our proposed matrix-free $\mathbf{K}\mathbf{x}$ kernel against the Deal.II 9.7.1 matrix-free implementation [49], which uses Kokkos 4.7.01 [50] as its GPU backend. Our implementation achieves a 5.86 \times higher throughput on 32 nodes (384 GPUs) of Aurora. While a prior GPU-optimized matrix-free kernel was introduced in [34]

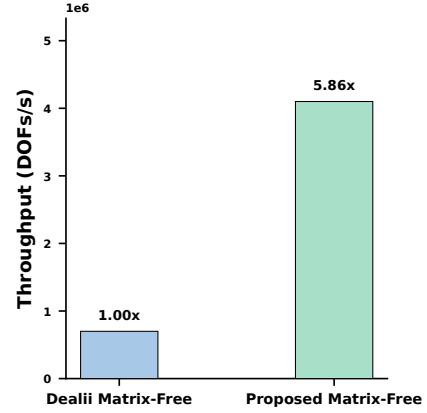


Fig. 5: Throughput (DOFs/s) comparison between the proposed matrix-free $\mathbf{K}\mathbf{x}$ kernel and the Deal.II 9.7.1 (Kokkos 4.7.01) implementation in the proposed preconditioned conjugate gradient solver.

with comparable speedup, the present implementation adopts a register-shared memory hybrid strategy that significantly reduces shared memory consumption per thread block. This increases thread block occupancy and, crucially, enables the use of higher finite-element polynomial orders that would otherwise exceed shared memory capacity.

D. Low precision computation and compressed communication leveraging R-ChFSI

Table II demonstrates the robustness of R-ChFSI-enabled mixed-precision computation and compressed communication for the 732-atom FGT system on 256 Aurora nodes (3072 GPUs). The wall time reported is the full time for the ground-state solve, excluding one-time initialization costs. The FP64/FP64 baseline converges in 66 SCF iterations with 69 total Chebyshev filtering passes. Using FP32(TF32) computation with BPV12-compressed communication, the solver converges in 68 SCFs with 74 passes—only 2 additional SCF iterations—while achieving a 2.27 \times reduction in SCF solve wall time (from 5503 s to 2427 s). The energy per atom difference between the two configurations is $\sim 1.3 \times 10^{-10}$ Ha/atom, confirming that the mixed-precision strategy preserves double-precision accuracy.

TABLE II: Convergence of the 732-atom FGT system on 256 Aurora nodes with different compute/communication precision configurations. All runs use R-ChFSI. Wall time is the SCF solve time excluding initialization. ΔE is the energy per atom difference relative to the FP64/FP64 baseline.

Compute/Comm.	Passes	SCFs	Wall time (s)	ΔE (Ha/atom)
FP64/FP64	69	66	5503	—
FP32(TF32)/BPV12	74	68	2427	1.3×10^{-10}

Figure 6 compares the speedup relative to the FP64/FP64 baseline across four node configurations (X, 2X, 4X, and 8X) for problem sizes $N = 32, 64, 128,$ and 256 , respectively. Three compressed communication configurations are evaluated: TF32/BPV16, TF32/BPV12, and TF32/BPV10, against the FP64/FP64 baseline (TF32/FP32 (32 nodes) is included for reference). The use of BFP compression provides consistent performance improvements for Chebyshev filtering (CF),

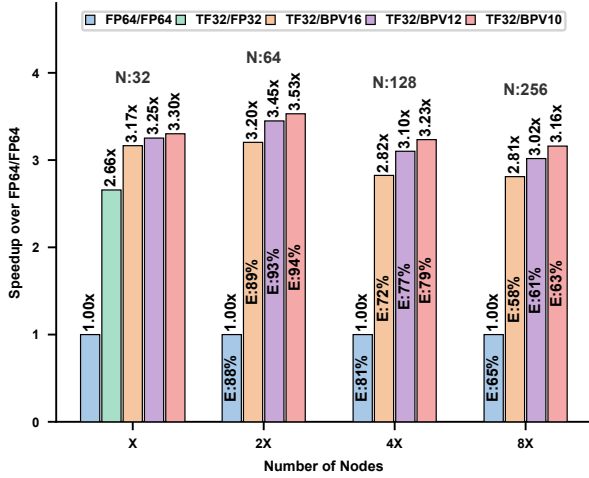


Fig. 6: Speedup of Chebyshev filtering (CF) using mixed-precision computation and reduced-precision communication. Speedups for CF, obtained with FP32 computation (using TF32 GEMMs) and compressed communication at varying bits per value (BPV), are shown relative to the FP64 compute-and-communication baseline, with values indicated above the bars for each node count (N). The scaling efficiency (E) for each compute/communication configuration, relative to the minimum node count (32), is also reported.

with peak speedups of up to $3.45\times$ and $3.53\times$ achieved by TF32/BPV12 and TF32/BPV10, respectively, at the 2X node configuration. The parallel efficiency, annotated on each bar, remains comparable to the FP64/FP64 baseline across all configurations.

E. Band-partitioning strategy

To improve the scaling efficiency of the Chebyshev filtering (CF) at extreme scaling regime, we employ band-partitioning strategy with $n_c = 8$ for the 256-node (8X) and 384-node (12X) runs. Results are compared against the TF32/BPV12 baseline ($n_c = 1$) at 32 nodes. Figure 7 shows that the CF scaling efficiency for the baseline ($n_c = 1$) drops to 60% at 8X and 45% at 12X node count. Band-partitioning strategy with $n_c = 8$ recovers this dramatically — to 97% at 8X and 94% at 12X — achieving a peak CF speedup of $11.34\times$ over the baseline at 12X nodes. Scaling efficiency measured across the full SCF iteration also benefits, though the growing gap between CF and SCF iteration efficiency at scale suggests that other parts of SCF iteration become the dominant bottleneck.

F. Performance studies on large-scale systems

Table III reports the per-SCF-iteration wall time breakdown for the two twisted bilayer MoSe₂ systems. The 4,326-atom system (37,492 electrons) was run on 256 Aurora nodes (3,072 GPUs), and the 9,114-atom system (78,988 electrons) on 800 Aurora nodes (9,600 GPUs). Wall times are reported for a representative SCF iteration (the 2nd, after initial subspace construction).

For the 37k-electron system, the mixed-precision configuration reduces the Chebyshev filtering time from 165 s to 60 s ($2.75\times$ speedup). The RR times show some variation between runs (116 s vs 99 s) due to the somewhat unstable

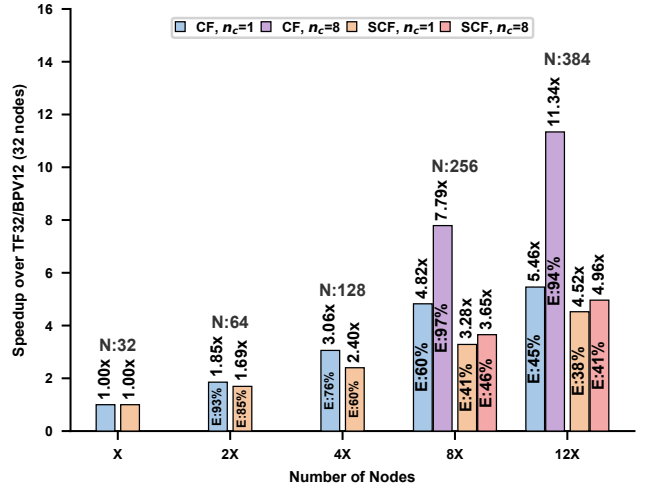


Fig. 7: Scaling efficiency of the Chebyshev filtering (CF) and a single SCF iteration using the band-partitioning strategy ($n_c = 8$) at 256 and 384 nodes. Speedups are measured relative to the TF32/BPV12 baseline at 32 nodes ($n_c = 1$) across increasing node counts (X through 12X). Scaling efficiency (E) is annotated on each bar.

nature of Aurora collectives at present. The overall per-SCF wall time reduces from 291 s to 169 s ($1.72\times$). For the larger 79k-electron system on 800 nodes, the filtering time drops from 333 s to 108 s ($3.09\times$), but the RR step dominates at this scale, consuming 636 s (FP64) and 540 s (TF32/BPV12) per SCF iteration. The large RR time at this node count is due to communication inefficiencies in the dense linear algebra collectives (ELPA eigensolver and distributed GEMM operations) on Aurora.¹ Despite this, the overall per-SCF wall time still improves from 1030 s to 691 s ($1.49\times$).

TABLE III: Per-SCF-iteration wall time breakdown (in seconds) for the twisted bilayer MoSe₂ systems. CG denotes the Poisson solves for electrostatics, CF the Chebyshev filtering, and RR the Rayleigh–Ritz step (projection, diagonalization, and subspace rotation).

System	Config.	CG	CF	RR	Total
MoSe ₂ 37k e^- (256 nodes)	FP64/FP64	1.4	165	116	291
	FP32(TF32)/BPV12	1.4	60	99	169
MoSe ₂ 79k e^- (800 nodes)	FP64/FP64	8.9	333	636	1030
	FP32(TF32)/BPV12	10.6	108	540	691

V. CONCLUSION

We present a GPU-accelerated framework for large-scale fully relativistic pseudopotential DFT calculations. A matrix-free Kx kernel exploiting tensor-product structure and a register-shared memory hybrid achieves $5.86\times$ higher throughput over Deal.II 9.7.1. R-ChFSI tolerates inexact matrix-vector products, enabling FP32/TF32 mixed-precision GEMMs and BFP-compressed MPI communication that deliver up to $3.53\times$ speedup in Chebyshev filtering and $2.27\times$ reduction in SCF wall time. With 2D band-partitioned strong scaling, the framework targets Fe₃GeTe₂ (732 atoms) and MoSe₂ twisted bilayers (up to 9,114 atoms, 78,988 electrons) on Aurora, enabling NC-SOC-DFT at $\mathcal{O}(10^5)$ electrons.

¹We are actively working with ALCF staff to resolve these bottlenecks

The performance advantages scale with system size: band-partitioning and R-ChFSI gain efficiency as domain decomposition saturates, and mixed-precision savings grow with the spinor subspace dimension. At smaller scales (~ 500 – 2000 electrons), simpler parallelization and standard double-precision ChFSI may suffice. The mixed-precision benefit depends on the FP32/TF64 versus FP64 throughput ratio — future GPU generations with stronger tensor core acceleration stand to gain more. On CPU-only architectures, mixed-precision advantages diminish, but the matrix-free and band-partitioning strategies remain effective.

REFERENCES

- [1] F. Gygi, E. W. Draeger, M. Schulz, B. R. De Supinski, J. A. Gunnels, V. Austel, J. C. Sexton, F. Franchetti, S. Kral, C. W. Ueberhuber *et al.*, “Large-scale electronic structure calculations of high-Z metals on the BlueGene/L platform,” in *Proceedings of the 2006 ACM/IEEE conference on Supercomputing*, 2006, pp. 45–es. [Online]. Available: <https://doi.org/10.1145/1188455.1188504>
- [2] G. Alvarez, M. S. Summers, D. E. Maxwell, M. Eisenbach, J. S. Meredith, J. M. Larkin, J. Levesque, T. A. Maier, P. R. Kent, E. F. D’Azevedo *et al.*, “New algorithm to enable 400+ TFlop/s sustained performance in simulations of disorder effects in high- T_c superconductors,” in *SC’08: Proceedings of the 2008 ACM/IEEE Conference on Supercomputing*. IEEE, 2008, pp. 1–10. [Online]. Available: <https://doi.org/10.1109/SC.2008.5214359>
- [3] Y. Hasegawa, J.-I. Iwata, M. Tsuji, D. Takahashi, A. Oshiyama, K. Minami, T. Boku, F. Shoji, A. Uno, M. Kurokawa *et al.*, “First-principles calculations of electron states of a silicon nanowire with 100,000 atoms on the K computer,” in *Proceedings of 2011 International Conference for High Performance Computing, Networking, Storage and Analysis*, 2011, pp. 1–11. [Online]. Available: <https://doi.org/10.1145/2063384.2063386>
- [4] A. N. Ziogas, T. Ben-Nun, G. I. Fernández, T. Schneider, M. Luisier, and T. Hoefler, “A data-centric approach to extreme-scale ab initio dissipative quantum transport simulations,” in *Proceedings of the International Conference for High Performance Computing, Networking, Storage and Analysis*, 2019, pp. 1–13. [Online]. Available: <https://doi.org/10.1145/3295500.3356156>
- [5] S. Das, B. Kanungo, V. Subramanian, G. Panigrahi, P. Motamarri, D. Rogers, P. Zimmermann, and V. Gavini, “Large-scale materials modeling at quantum accuracy: Ab initio simulations of quasicrystals and interacting extended defects in metallic alloys,” in *Proceedings of the International Conference for High Performance Computing, Networking, Storage and Analysis*, ser. SC ’23. New York, NY, USA: Association for Computing Machinery, 2023. [Online]. Available: <https://doi.org/10.1145/3581784.3627037>
- [6] J.-L. Fattebert, D. Osei-Kuffuor, E. W. Draeger, T. Ogitsu, and W. D. Krauss, “Modeling dilute solutions using first-principles molecular dynamics: computing more than a million atoms with over a million cores,” in *SC’16: Proceedings of the International Conference for High Performance Computing, Networking, Storage and Analysis*. IEEE, 2016, pp. 12–22. [Online]. Available: <https://doi.org/10.1109/SC.2016.2>
- [7] S. Das, P. Motamarri, V. Gavini, B. Turcksin, Y. W. Li, and B. Leback, “Fast, scalable and accurate finite-element based ab initio calculations using mixed precision computing: 46 PFLOPS simulation of a metallic dislocation system,” in *Proceedings of the International Conference for High Performance Computing, Networking, Storage and Analysis*, 2019, pp. 1–11. [Online]. Available: <https://doi.org/10.1145/3295500.3357157>
- [8] P. Hohenberg and W. Kohn, “Inhomogeneous electron gas,” *Phys. Rev.*, vol. 136, pp. B864–B871, 1964. [Online]. Available: <https://doi.org/10.1103/PhysRev.136.B864>
- [9] W. Kohn and L. J. Sham, “Self-consistent equations including exchange and correlation effects,” *Phys. Rev.*, vol. 140, pp. 1133–1138, 1965. [Online]. Available: <https://doi.org/10.1103/PhysRev.140.A1133>
- [10] <https://www.nobelprize.org/prizes/chemistry/1998/summary>. [Online]. Available: <https://www.nobelprize.org/prizes/chemistry/1998/summary>
- [11] S. Goedecker, “Linear scaling electronic structure methods,” *Rev. Mod. Phys.*, vol. 71, pp. 1085–1123, Jul 1999. [Online]. Available: <https://link.aps.org/doi/10.1103/RevModPhys.71.1085>
- [12] C.-K. Skylaris, P. D. Haynes, A. A. Mostofi, and M. C. Payne, “Introducing ONETEP: Linear-scaling density functional simulations on parallel computers,” *J. Chem. Phys.*, vol. 122, no. 8, p. 084119, 2005. [Online]. Available: <https://doi.org/10.1063/1.1839852>
- [13] D. Bowler and T. Miyazaki, “Methods in electronic structure calculations,” *Rep. Prog. Phys.*, vol. 75, no. 3, p. 036503, 2012. [Online]. Available: <https://doi.org/10.1088/0034-4885/75/3/036503>
- [14] L.-W. Wang, Z. Zhao, and J. Meza, “Linear-scaling three-dimensional fragment method for large-scale electronic structure calculations,” *Phys. Rev. B*, vol. 77, no. 16, p. 165113, 2008. [Online]. Available: <https://doi.org/10.1103/PhysRevB.77.165113>
- [15] M. Eisenbach, C.-G. Zhou, D. M. Nicholson, G. Brown, J. Larkin, and T. C. Schulthess, “A scalable method for ab initio computation of free energies in nanoscale systems,” in *Proceedings of the Conference on High Performance Computing Networking, Storage and Analysis*, 2009, pp. 1–8. [Online]. Available: <https://doi.org/10.1145/1654059.1654062>
- [16] R. Baer, D. Neuhauser, and E. Rabani, “Self-averaging stochastic Kohn-Sham density-functional theory,” *Phys. Rev. Lett.*, vol. 111, p. 106402, 2013. [Online]. Available: <https://doi.org/10.1103/PhysRevLett.111.106402>
- [17] M. D. Fabian, B. Shpiro, E. Rabani, D. Neuhauser, and R. Baer, “Stochastic density functional theory,” *WIREs Comput. Mol. Sci.*, vol. 9, no. 6, p. e1412, 2019. [Online]. Available: <https://doi.org/10.1002/wcms.1412>
- [18] S. Das, P. Motamarri, V. Subramanian, D. M. Rogers, and V. Gavini, “DFT-FE 1.0: A massively parallel hybrid CPU-GPU density functional theory code using finite-element discretization,” *Comput. Phys. Commun.*, vol. 280, p. 108473, 2022. [Online]. Available: <https://doi.org/10.1016/j.cpc.2022.108473>
- [19] J. Kübler, K. H. Hock, J. Sticht, and A. R. Williams, “Density functional theory of non-collinear magnetism,” *J. Phys. F: Met. Phys.*, vol. 18, pp. 469–483, 1988. [Online]. Available: <https://doi.org/10.1088/0305-4608/18/3/018>
- [20] U. von Barth and L. Hedin, “A local exchange-correlation potential for the spin polarized case. I,” *J. Phys. C: Solid State Phys.*, vol. 5, pp. 1629–1642, 1972. [Online]. Available: <https://doi.org/10.1088/0022-3719/5/13/012>
- [21] P. Motamarri, S. Das, S. Rudraraju, K. Ghosh, D. Davydov, and V. Gavini, “DFT-FE—a massively parallel adaptive finite-element code for large-scale density functional theory calculations,” *Comput. Phys. Commun.*, vol. 246, p. 106853, 2020. [Online]. Available: <https://doi.org/10.1016/j.cpc.2019.07.016>
- [22] D. R. Hamann, “Optimized norm-conserving Vanderbilt pseudopotentials,” *Phys. Rev. B*, vol. 88, p. 085117, Aug 2013. [Online]. Available: <https://doi.org/10.1103/PhysRevB.88.085117>
- [23] A. Dal Corso and A. M. Conte, “Spin-orbit coupling with ultrasoft pseudopotentials: Application to Au and Pt,” *Phys. Rev. B*, vol. 71, p. 115106, 2005. [Online]. Available: <https://doi.org/10.1103/PhysRevB.71.115106>
- [24] G. Kresse and J. Furthmüller, “Efficient iterative schemes for ab initio total-energy calculations using a plane-wave basis set,” *Phys. Rev. B*, vol. 54, no. 16, p. 11169, 1996. [Online]. Available: <https://doi.org/10.1103/PhysRevB.54.11169>
- [25] P. Giannozzi, O. Andreussi, T. Brumme, O. Bunau, M. B. Nardelli, M. Calandra, R. Car, C. Cavazzoni, D. Ceresoli, M. Cococcioni *et al.*, “Advanced capabilities for materials modelling with Quantum ESPRESSO,” *J. Phys.: Condens. Matter*, vol. 29, no. 46, p. 465901, 2017. [Online]. Available: <https://doi.org/10.1088/1361-648X/aa8f79>
- [26] J. R. Chelikowsky, N. Troullier, and Y. Saad, “Finite-difference-pseudopotential method: electronic structure calculations without a basis,” *Phys. Rev. Lett.*, vol. 72, no. 8, p. 1240, 1994. [Online]. Available: <https://doi.org/10.1103/PhysRevLett.72.1240>
- [27] L. Kronik, A. Makmal, M. L. Tiago, M. Alemany, M. Jain, X. Huang, Y. Saad, and J. R. Chelikowsky, “PARSEC—the pseudopotential algorithm for real-space electronic structure calculations: recent advances and novel applications to nano-structures,” *Phys. Status Solidi B*, vol. 243, no. 5, pp. 1063–1079, 2006. [Online]. Available: <https://doi.org/10.1002/pssb.200541463>
- [28] L. Genovese, A. Neelov, S. Goedecker, T. Deutsch, S. A. Ghasemi, A. Willand, D. Caliste, O. Zilberberg, M. Rayson, A. Bergman, and R. Schneider, “Daubechies wavelets as a basis set for density functional pseudopotential calculations,” *J. Chem. Phys.*, vol. 129, p. 014109, 2008. [Online]. Available: <https://doi.org/10.1063/1.2949547>

- [29] E. Tsuchida and M. Tsukada, "Adaptive finite-element method for electronic-structure calculations," *Phys. Rev. B*, vol. 54, no. 11, pp. 7602–7605, 1996. [Online]. Available: <https://doi.org/10.1103/PhysRevB.54.7602>
- [30] J. Pask and P. Sterne, "Finite element methods in ab initio electronic structure calculations," *Modell. Simul. Mater. Sci. Eng.*, vol. 13, no. 3, p. R71, 2005. [Online]. Available: <https://doi.org/10.1088/0965-0393/13/3/R01>
- [31] P. Motamarri, M. R. Nowak, K. Leiter, J. Knap, and V. Gavini, "Higher-order adaptive finite-element methods for Kohn–Sham density functional theory," *J. Comput. Phys.*, vol. 253, pp. 308–343, 2013. [Online]. Available: <https://doi.org/10.1016/j.jcp.2013.06.042>
- [32] D. Davydov, J.-P. Pelteret, D. Arndt, M. Kronbichler, and P. Steinmann, "A matrix-free approach for finite-strain hyperelastic problems using geometric multigrid," *Int. J. Numer. Methods Eng.*, vol. 121, no. 13, pp. 2874–2895, 2020. [Online]. Available: <https://doi.org/10.1002/nme.6336>
- [33] P. Fischer, M. Min, T. Rathnayake, S. Dutta, T. Kolev, V. Dobrev, J.-S. Camier, M. Kronbichler, T. Warburton, K. Świrydowicz, and J. Brown, "Scalability of high-performance PDE solvers," *Int. J. High Perform. Comput. Appl.*, vol. 34, no. 5, pp. 562–586, 2020. [Online]. Available: <https://doi.org/10.1177/1094342020915762>
- [34] G. Panigrahi, N. Kodali, D. Panda, and P. Motamarri, "Fast hardware-aware matrix-free algorithms for higher-order finite-element discretized matrix multivector products on distributed systems," *J. Parallel Distrib. Comput.*, vol. 192, p. 104925, 2024. [Online]. Available: <https://doi.org/10.1016/j.jpdc.2024.104925>
- [35] Z. He and H. Weng, "Giant nonlinear Hall effect in twisted bilayer WTe_2 ," *npj Quantum Mater.*, vol. 6, p. 101, 2021. [Online]. Available: <https://doi.org/10.1038/s41535-021-00403-9>
- [36] N. Kodali and P. Motamarri, "Finite-element methods for noncollinear magnetism and spin-orbit coupling in real-space pseudopotential density functional theory," *Phys. Rev. B*, vol. 111, p. 195129, May 2025. [Online]. Available: <https://link.aps.org/doi/10.1103/PhysRevB.111.195129>
- [37] J. Kim and M. M. May, "Resta-like preconditioning for self-consistent field iterations in the linearized augmented planewave method," *Electronic Structure*, vol. 4, no. 4, p. 047003, nov 2022. [Online]. Available: <https://doi.org/10.1088/2516-1075/aca24a>
- [38] Y. Zhou, Y. Saad, M. L. Tiago, and J. R. Chelikowsky, "Self-consistent-field calculations using Chebyshev-filtered subspace iteration," *J. Comput. Phys.*, vol. 219, no. 1, pp. 172 – 184, 2006. [Online]. Available: <https://doi.org/10.1016/j.jcp.2006.03.017>
- [39] N. Kodali, K. Ramakrishnan, and P. Motamarri, "Residual-based Chebyshev filtered subspace iteration for sparse Hermitian eigenvalue problems tolerant to inexact matrix-vector products," *arXiv preprint arXiv:2503.22652*, 2025. [Online]. Available: <https://arxiv.org/abs/2503.22652>
- [40] P. Lindstrom, "Fixed-rate compressed floating-point arrays," *IEEE Transactions on Visualization and Computer Graphics*, vol. 20, no. 12, pp. 2674–2683, 2014. [Online]. Available: <https://doi.org/10.1109/TVCG.2014.2346458>
- [41] W. E. Allcock, B. S. Allen, J. Anchell, V. Anisimov, T. Applencourt, A. Bagussetty, R. Balakrishnan, R. Balin, S. Bekele, C. Bertoni, C. Blackworth, R. Bustamante, K. Canada, J. Carrier, C. Chan-nui, L. C. Cheney, T. Childers, P. Coffman, S. Coghlan, T. Dey, M. D’Mello, A. Emani, M. Emani, K. G. Felker, S. Foreman, O. Franza, L. Gao, M. García, M. Garzarán, B. Gerofi, Y. Ghadar, S. Goswami, N. Gupta, K. Harms, V. Hatanpää, B. Holland, C. Holohan, B. Homerding, K. Hossain, X. Hu, L. Huot, H. Ibeid, J. A. Insley, S. Jayanthi, H. Jiang, W. Jiang, X.-Y. Jin, J. Kim, C. Knight, P. Kourdis, K. Kumaran, J. Kwack, J. Lee, T. Leggett, B. Lenard, C. Lewis, N. Liber, J. Lombardi, R. M. Loy, Y. Luo, B. Lusch, N. Mahadevan, B. Markey, V. A. Mateevitsi, G. McPheeters, R. Milner, J. Mitchell, V. A. Morozov, S. Muralidharan, T. Musta, M. Nagar, V. Narayana, M. Ngom, A.-T. Nguyen, N. Nichols, A. Nishtala, J. C. Osborn, M. E. Papka, S. Parker, S. S. Patel, J. Piotrowska, A. C. Pope, S. Raghunanda, E. Rangel, P. M. Rich, K. M. Riley, S. Rizzi, K. Rowe, V. Sastry, A. Scovel, F. Simini, H. S. Som, P. Steinbrecher, R. Stevens, X. Tian, P. Upton, T. Uram, A. K. Vasan, Álvaro Vázquez-Mayagoitia, K. Velusamy, B. Videau, V. Vishwanath, B. Whitney, T. J. Williams, M. Woodacre, S. Zeltner, C. Zhang, G. Zheng, and H. Zheng, "Aurora: Architecting argonne’s first exascale supercomputer for accelerated scientific discovery," 2025. [Online]. Available: <https://arxiv.org/abs/2509.08207>
- [42] Z. Fei, B. Huang, P. Malinowski, W. Wang, T. Song, J. Sanchez, W. Yao, D. Xiao, X. Zhu, A. F. May, W. Wu, D. H. Cobden, J. H. Chu, and X. Xu, "Two-dimensional itinerant ferromagnetism in atomically thin Fe_3GeTe_2 ," *Nat. Mater.*, vol. 17, no. 9, pp. 778–782, 2018. [Online]. Available: <https://doi.org/10.1038/s41563-018-0149-7>
- [43] Y. Deng, Y. Yu, Y. Song, J. Zhang, N. Z. Wang, Z. Sun, Y. Yi, Y. Z. Wu, S. Wu, J. Zhu, J. Wang, X. H. Chen, and Y. Zhang, "Gate-tunable room-temperature ferromagnetism in two-dimensional Fe_3GeTe_2 ," *Nature*, vol. 563, no. 7729, pp. 94–99, 2018. [Online]. Available: <https://doi.org/10.1038/s41586-018-0626-9>
- [44] F. Wu, T. Lovorn, and A. H. MacDonald, "Topological exciton bands in moiré heterojunctions," *Phys. Rev. Lett.*, vol. 118, p. 147401, 2017. [Online]. Available: <https://doi.org/10.1103/PhysRevLett.118.147401>
- [45] K. L. Seyler, P. Rivera, H. Yu, N. P. Wilson, E. L. Ray, D. G. Mandrus, J. Yan, W. Yao, and X. Xu, "Signatures of moiré-trapped valley excitons in $\text{MoSe}_2/\text{WSe}_2$ heterobilayers," *Nature*, vol. 567, pp. 66–70, 2019. [Online]. Available: <https://doi.org/10.1038/s41586-019-0957-1>
- [46] M. H. Naik and M. Jain, "Twister: Construction and structural relaxation of commensurate moiré superlattices," *Comput. Phys. Commun.*, vol. 271, p. 108184, 2022. [Online]. Available: <https://doi.org/10.1016/j.cpc.2021.108184>
- [47] M. Schlipf and F. Gygi, "Optimization algorithm for the generation of ONCV pseudopotentials," *Comput. Phys. Commun.*, vol. 196, pp. 36–44, 2015. [Online]. Available: <https://doi.org/10.1016/j.cpc.2015.05.011>
- [48] J. P. Perdew, K. Burke, and M. Ernzerhof, "Generalized gradient approximation made simple," *Phys. Rev. Lett.*, vol. 77, pp. 3865–3868, Oct 1996. [Online]. Available: <https://doi.org/10.1103/PhysRevLett.77.3865>
- [49] D. Arndt, W. Bangerth, M. Bergbauer, B. Blais, M. Fehling, R. Gassmüller, T. Heister, L. Heltai, M. Kronbichler, M. Maier, P. Munch, S. Scheuerman, B. Turcksin, S. Uzunbajakau, D. Wells, and M. Wichrowski, "The deal.ii library, version 9.7," *Journal of Numerical Mathematics*, vol. 33, no. 4, pp. 403–415, 2025. [Online]. Available: <https://doi.org/10.1515/jnma-2025-0115>
- [50] C. Trott, L. Berger-Vergiat, D. Poliakoff, S. Rajamanickam, D. Lebrun-Grandie, J. Madsen, N. Al Awar, M. Gligoric, G. Shipman, and G. Womeldorff, "The kokkos ecosystem: Comprehensive performance portability for high performance computing," *Computing in Science Engineering*, vol. 23, no. 5, pp. 10–18, 2021. [Online]. Available: <https://doi.org/10.1109/MCSE.2021.3098509>